Frontiers of Environmental Science & Engineering
2025, 19(4): 54 https://doi.org/10.1007/s11783-025-1974-y

RESEARCH ARTICLE

Upcycling waste protein and heavy metal into single-atom catalytic gas diffusion electrode for CO_2 reduction

Baiqin Zhou, Zhida Li, Chunyue Zhang, Lu Lu ✉

State Key Laboratory of Urban Water Resource and Environment, School of Civil and Environmental Engineering, Harbin Institute of Technology, Shenzhen 518055, China

HIGHLIGHTS

- The utilization of waste proteins and heavy metals for CO_2 to CO conversion.
- Proteins atomically disperse Ni onto a gas diffusion electrode (GDE).
- Porous structure of GDE is capable of CO_2 diffusion and storage.
- N element is crucial to synthesize efficient Ni single atom catalysts (Ni SACs).
- GDE is composed of nanofibers with uniformly dispersed Ni SACs.

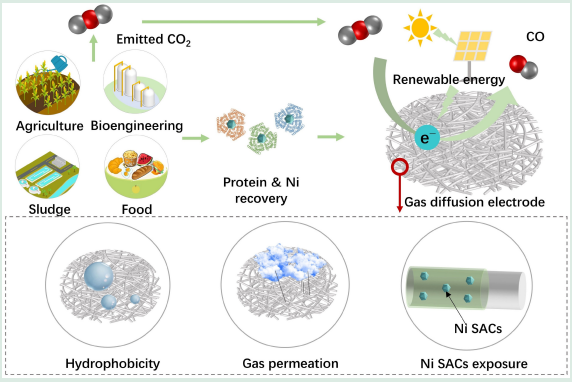

ABSTRACT: The global production of organic wastes and heavy metals (HMs) poses significant environmental risks, along with considerable carbon emissions from waste decomposition. This highlights the significance of synergistic management of both wastes and CO_2, which is a vital strategy for mitigating environmental pollution and climate change. Herein, we employed waste protein from wastewater produced during soybean peptide (SP) processing as a carbon matrix to anchor HMs Ni from electroplating wastewater. This mixture was electrospun into a gas diffusion electrode (GDE). This unique GDE design eliminates the need for a separate gas diffusion layer (GDL) and simplifies catalyst production. This versatile GDE consists of nanofibers with uniformly dispersed Ni single atom catalysts (SACs) on the fiber surface. Therefore, boasts a porous structure that facilitates CO_2 diffusion and storage. The homogeneous distribution of Ni SACs within the GDE fosters high activity in the electrochemical conversion of CO_2 to CO. At 50 mA/cm^2 and 2.5 V cell voltage, Ni SACs achieved an excellent Faradaic efficiency of 81%−98% in a membrane electrode assembly (MEA). This technique holds a promise in achieving the collaborative management of carbon mitigation and wastes recovery.

KEYWORDS: Waste protein, Heavy metal wastewater, Ni single atom, Electrospinning, Gas diffusion electrode, CO_2 reduction

✉ Corresponding author. E-mail: lulu@hit.edu.cn

Article history: Received 30 September 2024, Revised 30 November 2024, Accepted 13 January 2025, Available online 25 February 2025

1 Introduction

The pursuit of carbon neutrality in numerous countries has facilitated extensive research on carbon mitigation strategies in energy-intensive industries (Yuan et al., 2024). However, CO_2 emissions from organic wastes and wastewater have been understudied (Jones, 2013; Lu et al., 2018; Voosen, 2020; Reichstein et al., 2021; Xu et al., 2021; Liu et al., 2024). Studies have shown that organic waste and wastewater, particularly from agriculture and food industries, account for over 7% of global CO_2-equivalent emissions (Gustavsson et al., 2011; Mohareb et al., 2018; Yang et al., 2024). The electrochemical CO_2 reduction reaction (ECO_2RR) has recently exhibited significant potential for mitigating CO_2 emissions and producing valuable carbon-based chemicals (Sharifian et al., 2021). Therefore, directly converting waste-derived CO_2 into value-added products by ECO_2RR holds great promises for sustainable development. Beside the organic matters, heavy metals (HMs) may exist in the wastes, which is toxic but also exhibits catalyzing nature for chemical reactions (Gu et al., 2024). Here, we suppose whether soybean peptide (SP) processing wastewater and HMs derived from electroplating wastewater as the precursors of ECO_2RR catalysts could be feasible for simultaneous CO_2 mitigation and wastes treatment. We propose employing SP to fix HMs Ni in the wastewater, then the formed mixture was used to fabricate a gas diffusion electrode (GDE) with *in situ* growth of Ni single atoms (SAs) catalyst for low-cost CO_2-CO electrochemical conversion.

Developing efficient and low-cost electrocatalytic materials for converting CO_2 to CO rather than liquid products remains a challenge (Xia et al., 2019; Fan et al., 2020; Peng et al., 2021; Wang et al. 2024; Tan et al., 2025). Current research found that earth-abundant Ni single atom catalysts (SACs) can maximize the efficiency of catalytic sites to facilitate the conversion of CO_2 to CO (Jiang et al., 2018; Zheng et al., 2019; Li et al., 2020; Yang et al., 2020). Ni SACs are typically synthesized using Ni-contained salt and expensive carbon matrix, such as metal organic frameworks (MOFs) (Li et al., 2020; Yang et al., 2020; Sun et al., 2025), carbon nanotubes (CNTs) (Liang et al., 2021), and graphene (Jiang et al., 2018), etc. therefore, utilizing affordable carbon matrices is necessary for facilitating the large-scale production of Ni SACs. Previous studies have indicated the importance of N-element doping to enhance the Ni SACs performance, since the formed Ni-N_x during carbonization was proved to resist metals leaching (Liang et al., 2021) and improve the detachment of absorbed CO (CO*) due to the decreased binding energy (Liu et al., 2021; Qin et al. 2025). Consequently, we proposed the use of proteins, a widely available N-enriched matter, to synthesize SACs. In addition, proteins can effectively bind HMs on a uniform and ultrasmall scale through interactions such as chelation between functional groups and Ni atoms, electrostatic attraction, and van der Waals forces (Blundell and Jenkins, 1977; Ge et al., 2012). Moreover, the total amount of low-cost protein is considerable given the tremendous protein-enriched wastes produced annually, such as agriculture and food wastes. For example, Food and Agriculture Organization of the United Nations (FAO) statistics show that more than 3 billion tons of various food are wasted annually, corresponding to more than 0.24 billion tons of waste protein produced based on the protein contents in 7 main kinds of foods (Table S3, Table S) (Gustavsson et al., 2011). Therefore, there is a great potential to utilize the waste protein as carbon matrix to synthesize highly efficient catalysts for CO_2 conversion.

ECO_2RR is generally conducted in bulk electrolyte solution using a single chamber or H-type electrolysis cell (Figs. S1(a) and (b)), but low solubility (0.033 mol/L) and low diffusion (0.0016 mm^2/s) of CO_2 molecules in a bulk solution well confine ECO_2RR kinetics to a low level (Verma et al., 2016; Weekes et al., 2018; Nguyen and Dinh, 2020). Despite using HCO_3^-, more soluble and more diffusional in solution, as the feedstock to electro-conversion toward CO and formate have been reported (Li et al., 2019; Sun et al. 2024), the energy penalty and catalysts' cost were strikingly higher than the counterpart system of CO_2 as the feedstock. Feedstock for ECO_2RR remains preference toward CO_2 molecules. The resultant mass transfer limitation in bulk solution inflicts on current uplift to a commercially viable operation. Delivering humidified CO_2 gaseous, instead, for ECO_2RR serves as a solution against mass transfer limitation. Hike in (0.041 mol/L) and diffusion (16 mm^2/s) drives current density up to several hundred mA/cm^2, making a step toward large-scale application of ECO_2RR. (Weekes et al., 2018). Adaptative to humidified CO_2 gaseous feeding necessitates conversion from a traditional H-type or single chamber electrolysis cell to a membrane electrode assembly (MEA) (Figs. S1(c) and S1(d)). MEA is a contacted electrolysis cell where cathode, ion exchange and anode are clung, leaving zero gap within them. The linchpin in MEA is the gas diffusion electrode (GDE), providing a thin interface for gaseous CO_2 pass through while preventing bulk solution penetration. Traditionally, powdered catalysts are slathered onto a gas diffusion layer (GDL) to

manufacture a GDE, yet catalysts cannot resist to be stripped away via continuous electrolyte flourish, inflicting on GDE duration.

In this study, we originally used wasted protein to capture Ni in the real wastewater and directly converted the organic-HMs mixture into a Ni-SACs distributed gas diffusion electrode (GDE) through electrospinning coupled with carbonization. This tactic *in situ* synthesized Ni SACs onto the surface of nanofibers of GDE, avoiding tedious processes of fabricating GDL and catalyst separately to achieve an overwhelming stability and selectivity toward CO. The satisfactory CO selectivity remained no matter conducting ECO_2RR in a single-chamber or in a MEA. Despite the progress in the development of biomass-derived catalysts has been made, co-management of organic wastes, HMs and CO_2 emission have rarely been reported. Using herein static simultaneously reclaimed protein and HMs from wastes or wastewater, and driven overdue atmospheric CO_2 into non-greenhouse while value-added gas, pushing toward a closed carbon loop or even negative emission in wastes treatment as Fig. 1(a) showed.

2 Materials and methods

2.1 Source of the wastes

The wastewater produced from a soybean peptide (SP) processing factory in Shenzhen, China was selected as the source of waste protein to synthesize the GDE. The SP wastewater had a total soluble protein concentration of around 10000 mg/L (as measured by bicinchoninic acid assay) (Table S4). Heavy metals (HMs) contained wastewater was obtained from an electroplating factory in Meizhou, China with Ni (around 183 mg/L) as the dominant metal (Table S5).

2.2 Preparation of waste-derived GDE

The electrospinning technique was used to manufacture GDE with ultrafine nanofibers and ultrahigh porosity for gas diffusion and storage (Yang et al., 2019) (Fig. S2). SP processing wastewater was mixed with HMs-containing wastewater at a protein to Ni mass ratio of 50:1. A 12 wt% polyacrylonitrile (PAN) in solution was used as the flexible support material. These two solutions were simultaneously electrospun into fiber using 18−20 kV voltage applied to the syringe needle, while the collector was charged with −0.05 to −4 kV voltage. The syringe feed rate for both the PAN and SP solutions was set at 1 mL/h. After 45−50 h of operation, the synthesized membrane underwent peroxidation in a muffle furnace at 260 °C for 2 h and then cooled to room temperature. The following carbonization was conducted at 1000 °C for 2 h under argon atmosphere protection. The synthesized GDE was labeled as SP_{GDE}. For a comparison, we synthesized GDE using only PAN solution and Ni addition according to the same procedures. The resulting material was labeled as NP_{GDE}. To enhance the surface hydrophobicity of SP_{GDE}, 5 wt% Nafion 117 solution was drop-cast on SP_{GDE} (Yang et al., 2020).

2.3 Electrochemical measurements

To deeply examine the catalytic performance of GDE, we first ground GDEs into powder and then drop-cast the powder onto a carbon paper (Tory TGP-H-060). ECO_2RR was conducted in a single chamber electrolysis cell (Fig. S1(a)) using a 0.5 mol/L $KHCO_3$ solution as the electrolyte. An Ag/AgCl electrode was used as the reference electrode, and a platinum plate served as the counter electrode. The potential was expressed relative to the reversible hydrogen electrode (vs. RHE) using the following equation:

$$E \text{ vs. RHE} = E \text{ vs. Ag/AgCl} + 0.197 + 0.059 \times \text{pH} \quad (1)$$

ECO_2RR at high current density was conducted in a MEA that is consist of a GDE, an oxygen evolution electrode (IrO_2-coated titanium mesh, more details were provided in Supplementary Materials), flow plates, and a Nafion 117 membrane (Fig. S1(d)). The CO_2 flow was controlled by a mass flow meter (MC-100SCCM-D-DB9M, Alicat, USA) at 20 or 50 standard cubic centimeter per minute (sccm). The electrolyte flow was controlled by a peristaltic pump (BT100-2J, Dichuang, China) at 50 mL/min. All electrochemical measurements were conducted using a potentiostat (1010E, Gamry, USA).

2.4 Analysis and calculations

Gas products of CO_2RR were detected by a gas chromatograph (GC) (TRACE 1310, Thermo, USA) equipped with a thermal conductivity (TCD). The partial current density of individual products was calculated by the following formula:

$$j_i = x_i \times v \times z_i \times F \times P_0 \times \text{electrode area}/RT, \quad (2)$$

where x_i represents the volume fraction of a given gas product i, v is the flow rate, z_i is the number of transferred electrons, F is the Faraday constant, P_0 is 101.325 kPa, R is the gas constant, and T is the temperature. The corresponding Faradaic Efficiency (FE) was calculated as follows:

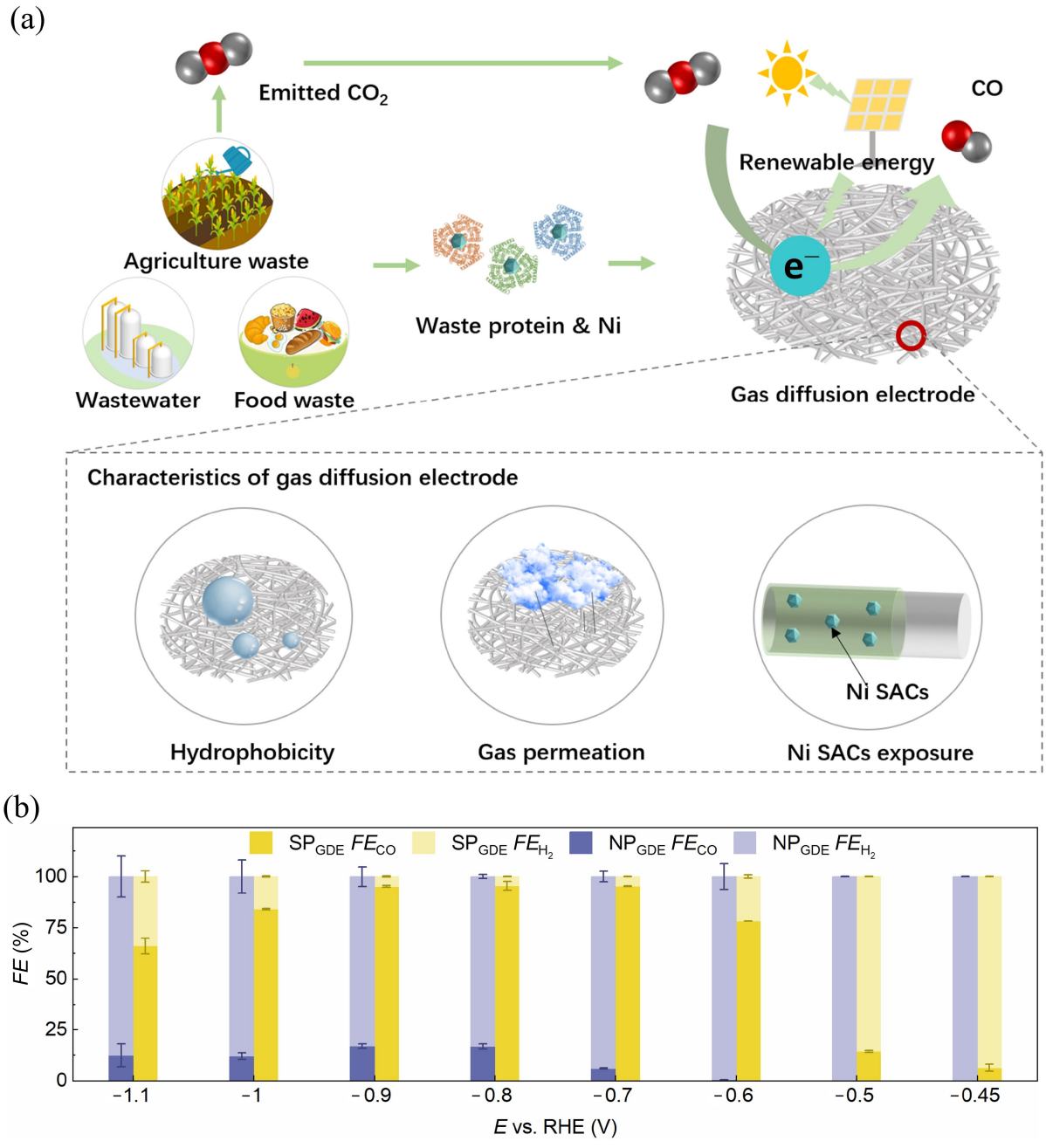

Fig. 1 Schematic of waste protein and Ni recovery for synthesis of Ni SACs-containing GDE for ECO_2RR. (a) Overview of the GDE synthesis and key characteristics, (b) CO and H_2 selectivity under different ECO_2RR potentials for GDEs synthesized with waste protein (SP_{GDE}) and without protein (NP_{GDE}).

$$FE = j_i / j_{total} \times 100\%, \quad (3)$$

the turnover frequency (TOFs, h^{-1}) for ECO_2RR products was evaluated based on the electrochemical active surface area (ECSA) normalization. Details in calculation can be found in Supplementary Materials (Jiang et al., 2018):

$$\text{TOFs} = (j_{total} \times t \times FE_{CO})/(2F \times \text{the number of Ni sites}). \quad (4)$$

Energy efficiency can be calculated as the follows:

$$\text{Energy efficiency} = (E^0 \times FE_{CO})/E_{cell}, \quad (5)$$

where $E^0 = E_{O_2} - E_{CO} = 1.23 - (-0.11) = 1.34$ V, with E_{O_2} and E_{CO} representing the O_2/H_2O and CO_2/CO

equilibrium potentials, respectively.

The potential protein amount that can be extracted from 7 kinds of agriculture and food waste was calculated based on the statistics of Food and Agriculture Organization of the United Nations (FAO) (Tables S2 to S3) (Gustavsson et al., 2011).

2.5 GDE characterizations

The morphology and structure of GDE were characterized via scanning electron microscopy (SEM, TESCAN MIRA4), transmission electron microscopy (TEM, FEI Talos F200X), aberration-corrected scanning transmission electron microscopy (STEM, Titan Cubed Themis G2300) and X-ray diffraction (XRD, RIGAKU Ultima IV). Chemical bonds and compositions were provided by Fourier Transform Infrared Spectrometer (FTIR, Scientific Nicolet iS20) and X-ray photoelectron spectroscopy (XPS, Scientific K-Alpha). The contact angle of GDE surface was observed by a contact angle testing analyzer (KRUSS DSA25). Porous structure, specific surface area and CO_2 adsorption capacity were examined by a BET analyzer (Micrometrics ASAP 2460) using N_2 and CO_2. Surface anti-wettability was detected by a Confocal Laser Scanning Microscope (Nikon AX-SHR). 1 mol/L KOH solution with dilute Rhodamine B served as the color reagent and a 488 nm laser was selected as the excitation source. Heavy metals concentration was detected by an inductively coupled plasma mass spectrometry (NexION 1000, PerkinElmer). Scanning electrochemical microscopy (Princeton Applied Research) was operated by applying GDE with −1.24 V vs. RHE and microelectrode with 0.2 V vs. RHE to consume evolved CO.

3 Results and discussion

3.1 Selectivity toward CO_2 to CO electrochemical conversion

The GC analysis confirmed that CO and H_2 were the predominant products generated during ECO_2RR using GDEs as catalysts. The absence of liquid products was further verified by ^1H NMR spectroscopy results (Fig. S3). The performance of SP_{GDE} in ECO_2RR was examined across a potential from −0.45 to −1.1 V vs. RHE (Fig. 1(b)). Notably, SP_{GDE} exhibited excellent selectivity, achieving FE_{CO} exceeding 80% across a broad potential range from −0.6 to −1.0 V vs. RHE, underscoring the superior CO_2 conversion efficiency of SP_{GDE} compared with NP_{GDE}. The maximum FE_{CO} is 96% at −0.8 V vs. RHE, while corresponding FE_{H_2} is below 4%. The minimum CO signal detected at −0.45 V vs. RHE by SP_{GDE} indicates that the onset overpotential is smaller than 340 mV which is notably lower than 490 mV required by NP_{GDE}. NP_{GDE} was more liable to carry out hydrogen evolution reaction (HER) rather than CO evolution with approximately 20% FE_{CO} at its optimal potential of −1.54 V vs. RHE.

3.2 GDE characterizations

Before carbonization, the pristine GDE exhibits an initial size of 200 cm^2, indicating its potential scalability (Fig. S2c). GDE with a thickness of ~400 μm, comprise interconnected fibers with diameters in the range of several hundred nanometers (Figs. 2(a)–2(c) and S4). The porous structure of GDE with a pore size distribution of 1–120 nm indicates the development of macropores, mesopores, and micropores during carbonization. These pores play distinct roles in CO_2 adsorption. Particularly, micropores (smaller than 20 nm) serve as primary adsorption sites for CO_2 molecules (kinetic diameter of 3.4 Å). Additionally, mesopores (20–50 nm) and macropores (larger than 50 nm) function as channels to facilitate gas transport. The CO_2 adsorption isotherm confirms that GDE can store CO_2 with a capacity of 4–7 cm^3 of CO_2/g-GDE under atmospheric pressure. Moreover, the BET analysis reveals negligible differences in CO_2 storage capacity between SP_{GDE} and NP_{GDE}, indicating that the introduction of SP does not influence the porous structure and CO_2 storage capacity. Hydrophobicity, a crucial factor influencing GDE performance, is significantly improved through the treatment of GDE (SP_{DGE} and NP_{GDE}) with a 5 wt% Nafion 117 solution (Yang et al., 2020), resulting in a water contact angle of 135.7° (Figs. 2(f) and S5). We further used a confocal laser scanning microscope to assess the penetration depth of a Rhodamine B water solution, highlighting the enhanced water resistance achieved through Nafion treatment. Notably, after Nafion treatment, the penetration depth of the Rhodamine B solution decreases from ~40 to ~20 μm, further confirming the improved hydrophobicity of the SP_{GDE} surface.

Before the analysis of chemical bonds, we first examined the structure of the Ni-containing SP protein. The XPS N 1s spectrum exhibits three split peaks at 398.3, 399.4, and 400.1 eV, corresponding to NH_2/NH_3 groups in SP proteins (Figs. 3(a) and S6). After Ni adsorption onto SP, the intensity of the peak at 399.4 eV significantly decreases, indicating the formation of coordination between N_x and Ni. This coordination is

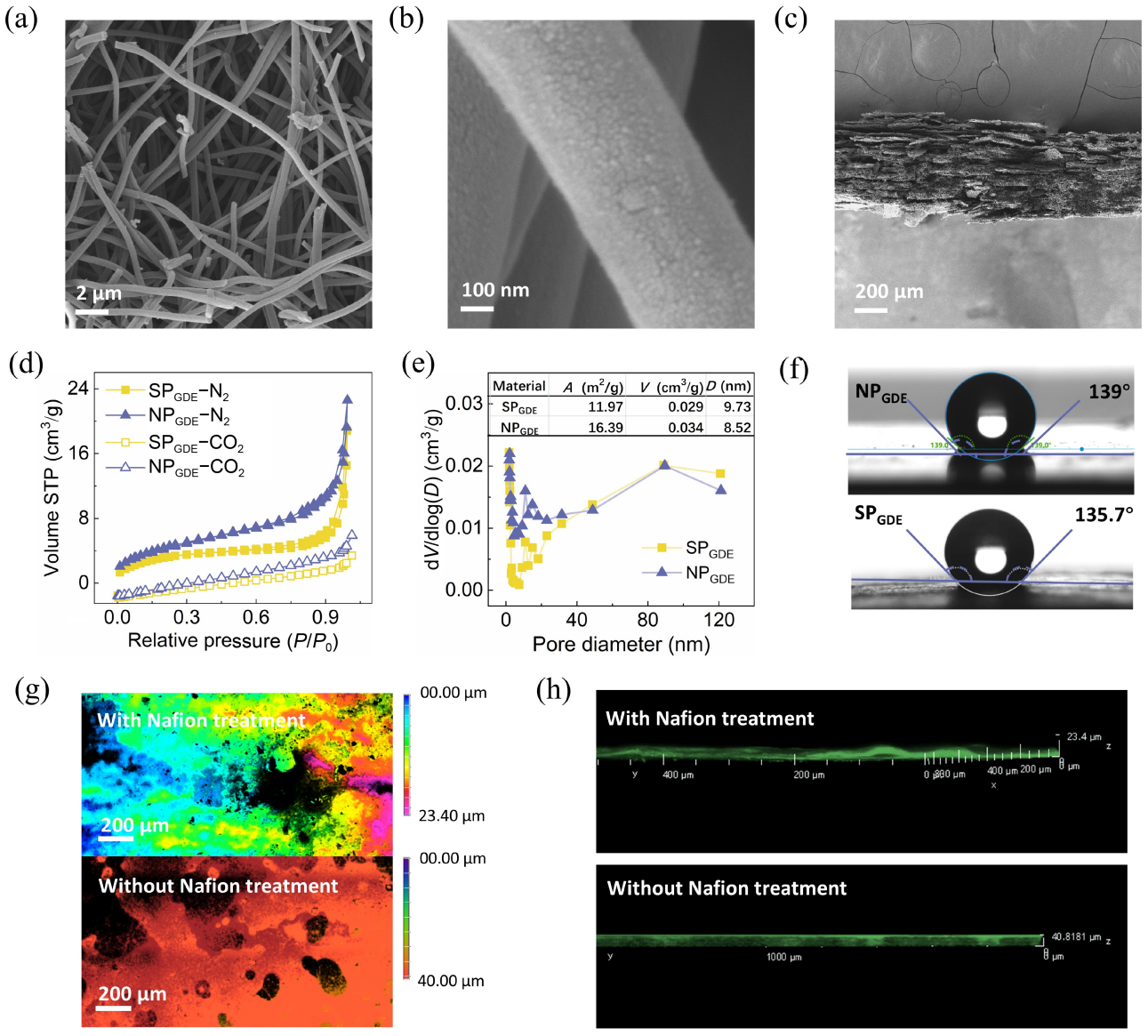

Fig. 2 Porous structure and hydrophobic surface of the GDE. SEM images of the SP_{GDE} (a) surface, (b) nanofibers and (c) cross section, (d) N_2 ad-desorption isotherm, (e) CO_2 storage ability and pore size distribution of the SP_{GDE} and NP_{GDE}, (f) Contact angle of SP_{GDE} and NP_{GDE} surface after 5 wt% Nafion treatment. (g) The planar and (h) cross-sectional photographs for penetration of water on SP_{GDE} detected by Confocal Laser Scanning Microscope (fluorescent dye is Rhodamine B).

considered a crucial catalytic site for CO_2 to CO conversion (Zheng et al., 2019; Yang et al., 2020; Yao et al. 2024; Qin et al. 2025). The emergence of Ni–S coordination (Fig. 3(b)) further indicates the formation of various complex structures between Ni and SP. In these complexes, Ni mainly exists as Ni^{2+} (Fig. 3(c)). After Ni adsorption, significant alterations were observed in the FTIR spectra. A series of changes observed around 1400 cm^{-1} (Fig. 3(d)) correspond to the symmetric stretching vibration of COO^-, indicating interactions between Ni and C-containing groups (Ye et al. 2025). Additionally, the peak around 2940 cm^{-1} is attributable to the symmetric stretching vibration of dispersed NH_2^+/NH_3^+, indicating a crucial complexation form between SP and HMs (Blundell and Jenkins, 1977; Weng and Xu, 2016).

After preoxidation and carbonization processes, differences between SP_{GDE} and NP_{GDE} are observed. The FTIR spectra of both SP_{GDE} and NP_{GDE} exhibit comparable peaks above 900 cm^{-1}, (Fig. 3(d)), with C–H stretching vibrations (990–1150 cm^{-1}) and C–N vibrations (1124 or 1219 cm^{-1}). However, significant

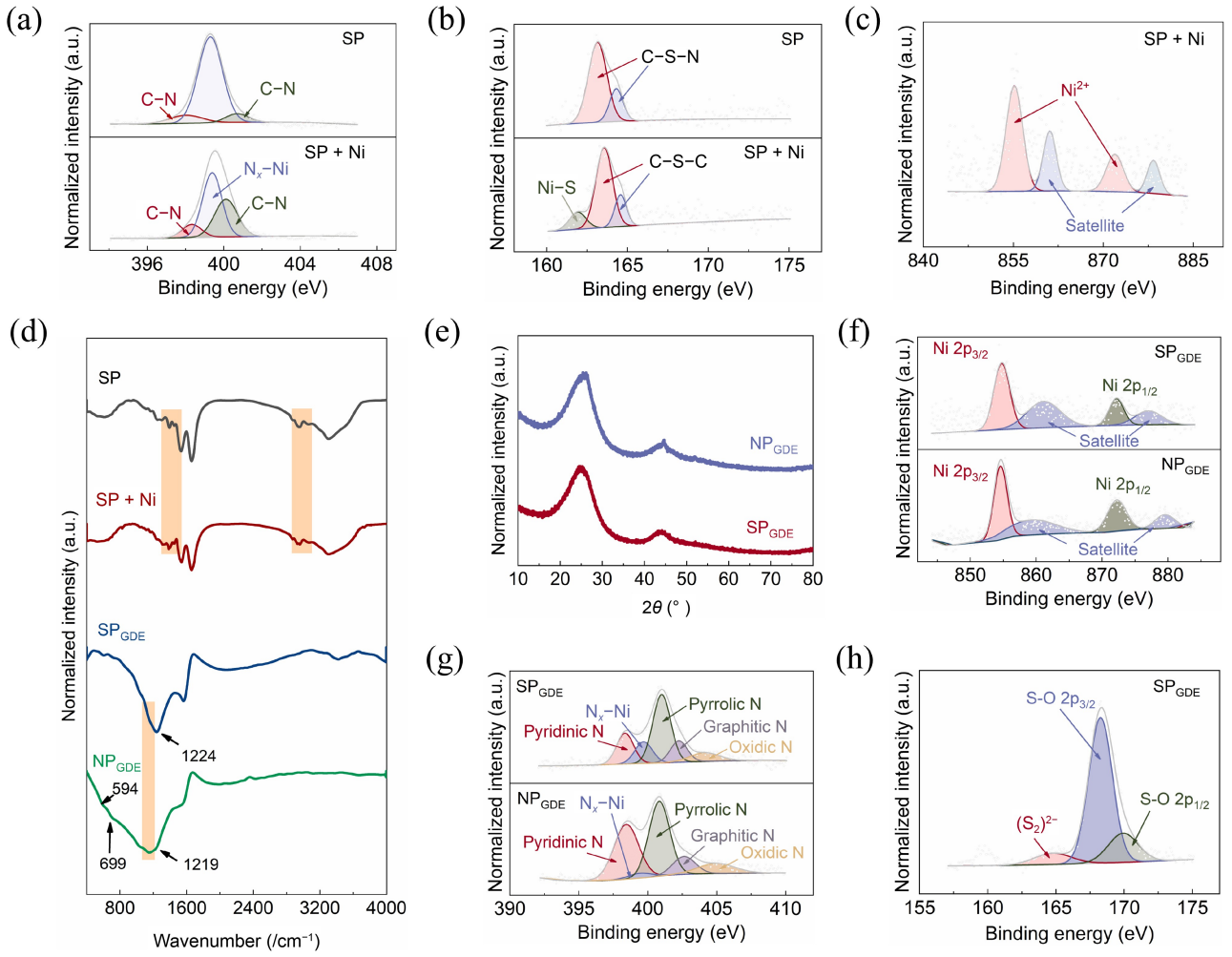

Fig. 3 Chemical compositions and chemical bonds of SP, SP + Ni, SP_{GDE} and NP_{GDE}. XPS splitting peaks of (a) N 1s, (b) S 2p and (c) Ni 2p for SP and SP + Ni. (d) FTIR spectra of SP, SP + Ni, SP_{GDE} and NP_{GDE}. (e) XRD spectra of SP_{GDE} and NP_{GDE}. XPS splitting peaks of (f) Ni 2p, (g) N 1s and (h) S 2p for SP_{GDE} and NP_{GDE}.

differences were observed in the lower absorbance region. Specifically, the FTIR spectrum of NP_{GDE} displays distinct peaks at 594 and 669 cm^{-1}, indicative of metal–O vibrations, suggesting interactions between Ni and oxygen-containing functional groups in NP_{GDE} (Weng and Xu, 2016). The XRD spectra of both SP_{GDE} and NP_{GDE} reveal a graphitic matrix and peaks at 26.2° and 44° (Fig. 3(e)), with no detection of other crystal phases. The XPS analysis confirms that the Ni content is below 1 at% (Fig. S7), consistent with previous reports on Ni SACs (Zheng et al., 2019; Yang et al., 2020; Yao et al. 2024; Qin et al. 2025). Additionally, no Ni^0 (853.5 eV) peak associated with Ni nanoparticles was detected (Fig. 3(f)). The N $2p_{3/2}$ spectrum (Fig. 3(h)) exhibits five typical peaks corresponding to pyridinic N (398.2 eV), N_x–Ni (399.4 eV), pyrrolic N (400.5 eV), graphitic N (401.3 eV), and oxidized N (403.0 eV) species in SP_{GDE}. Although both SP_{GDE} and NP_{GDE} contain similar Ni species, their N chemical forms differ. NP_{GDE} contains a smaller proportion of N_x–Ni and a higher pyridinic N content, which may reduce its conductivity of NP_{GDE} owing to the lower electron cloud density of pyridine (Zheng et al., 2019; Yang et al., 2020; Qin et al. 2025). The S–Ni coordination disappeared after carbonization (Figs. 3(b) and 3(h)), indicating that S–Ni is unstable during carbonization and cannot effectively disperse Ni SAs.

The nanofiber surface of SP_{GDE} exhibits a homogeneous structure with uniform dispersion of Ni and amorphous carbon as the matrix, and no Ni nanoparticles or clusters were detected either via SEM or TEM (Figs. 4 and S8, S9). The uniform dispersion of Ni and S elements onto the nanofiber surface suggests

that waste SP and Ni mainly attach to the surface of the PAN nanofibers rather than forming nanofibers during electrospinning. This behavior was consistent with our finding that an SP + Ni solution without PAN cannot form threadlike fibers during electrospinning, unlike PAN. The distribution of electrocatalytic sites on the SP_{GDE} surface (maintained at −0.6 V vs. RHE) was investigated using a scanning electrochemical microscopy system with a Pt ultramicroelectrode tip poised at 0.84 V vs. RHE. During the scanning of the SP_{GDE} surface, the tip oxidizes the ECO_2RR products (either CO or H_2) to generate a measurable current that visualizes electrochemical activity. The current distribution exhibits a wave-like pattern with a characteristic width of ~400 nm, consistent with the diameter of SP_{GDE} nanofibers. This indicates that

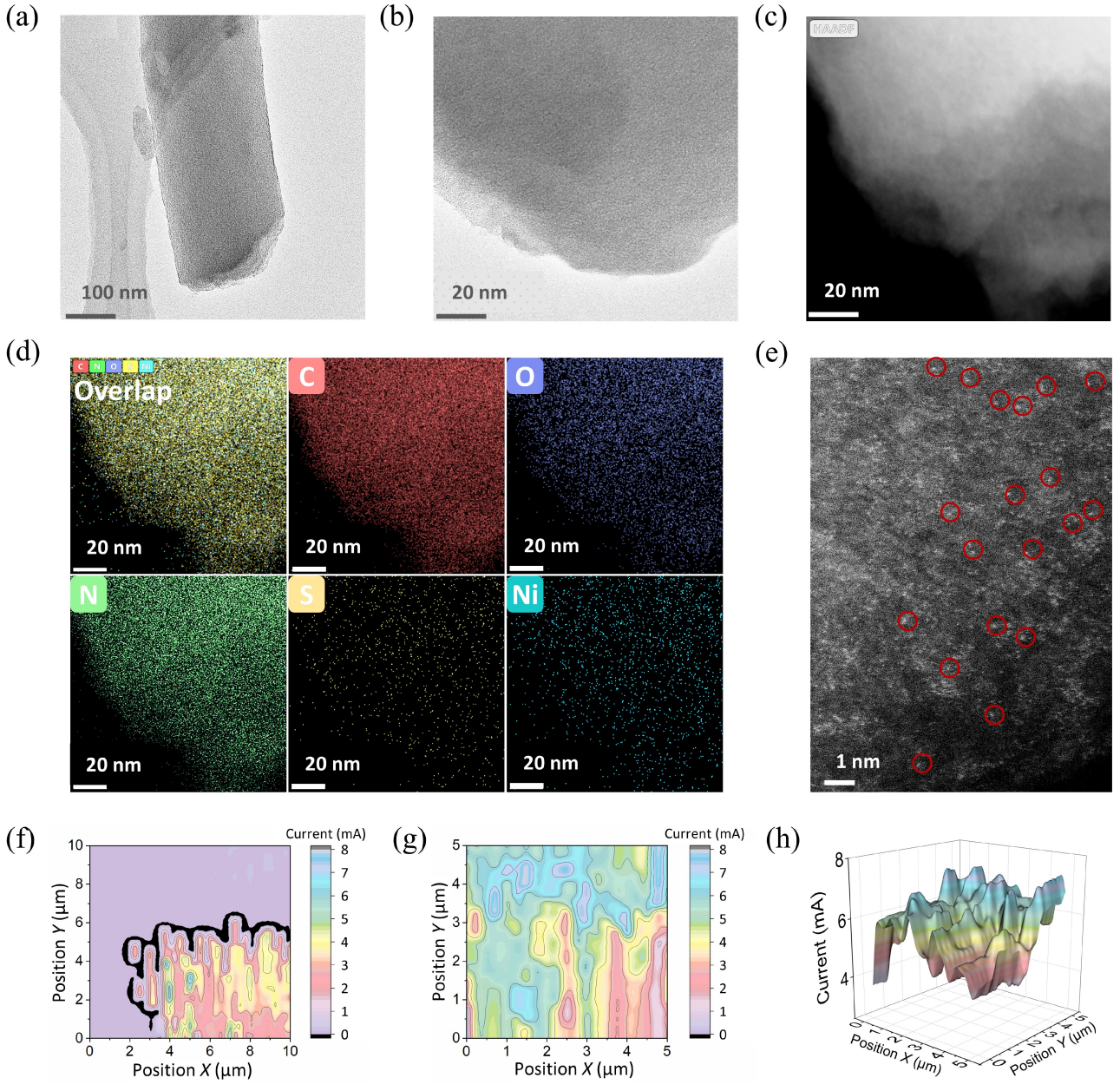

Fig. 4 Homogeneous Ni SAs distribution on the nanofiber of SP_{GDE}. (a) and (b) TEM images, (c) HAADF-STEM images and (d) corresponding elemental mappings, (e) AC-HAADF-STEM image of SP_{GDE} (the light dots in red cycle are Ni SAs). Scanning electrochemical microscopy images of (f) the border between SP_{GDE} and epoxy resin that is used to fix SP_{GDE} samples, (g) SP_{GDE} surface and (h) 3D hypsometric map of SP_{GDE} surface.

efficient electrocatalytic sites are efficiently distributed on the surface of each nanofiber (Figs. 4(f)–4(h), and S10). In contrast, the epoxy resin used to fix the SP_{GDE} samples produces negligible current signals, forming a distinct boundary with the SP_{GDE} material.

The nanofiber surface of NP_{GDE} is similar to that of SP_{GDE} (Figs. S11 and S12). However, nanoparticles with crystal cells were detected on the surface of some nanofibers via AC-HAADF-STEM (Fig. S13). These crystal cells exhibit distinguishable brightness compared with the surrounding carbon matrix. The corresponding elemental mapping displays Ni element agglomeration on these crystal cells. The ~0.2 nm fringe pattern indicates that these nanoparticles are pure Ni^0 nanoparticles. Ni SAs form at the nanofiber surface (Fig. S14). However, no Ni^0 peaks are observed in the XRD and XPS spectra of NP_{GDE} (Figs. 3(f) and 3(g)) owing to the low loading of Ni nanoparticles on the nanofibers. Generally, the electrospinning technique can homogeneously disperse Ni SAs onto a matrix. Nevertheless, owing to the agglomeration tendency of Ni, a dispersing agent (SP) is required to stabilize Ni in its atomic form.

3.3 ECO_2RR performance in a MEA

Ni SACs were successfully synthesized on both SP_{GDE} and NP_{GDE} surfaces. However, the presence of Ni nanoparticles on the NP_{GDE} surface affected its product selectivity compared with SP_{GDE}, as the Ni nanoparticles influenced HER even at low concentrations. Acid soaking is a common method for removing nanoparticles. The selectivity toward CO in NP_{GDE} increased with prolonged soaking time in 2 mol/L H_2SO_4 (Fig. S15). The FE_{CO} of SP_{GDE} slightly decreased with increasing soaking time. Notably, the non-treated SP_{GDE} exhibited the highest CO selectivity. This indicates that acid soaking is not required for SP_{GDE} owing to the absence of Ni nanoparticles on SP_{GDE} and the protective effect of the synthesis strategy on Ni SAs. At lower carbonization temperatures (700–800 °C), the synthesized SP_{GDE} exhibited favorable CO selectivity (Fig. S16). This suggests that SP_{GDE} synthesis requires a more moderate energy input compared with ZIF-8-derived Ni SACs, which are typically synthesized at higher temperatures (900–1000 °C) to volatilize residual Zn.

The TOFs (h) of SP_{GDE} for CO production at −1.1 V vs. RHE was measured as 10305.82 h^{-1} based on ECSA normalization (Fig. 5(a)), which is comparable to most reported values (Jiang et al., 2018; Zheng et al., 2019). TOFs reflect the number of catalytic sites occurring, the target products generated, and the reactants consumed per unit active site under temperature, pressure, reactant ratio, and reaction conditions. Moreover, TOFs represent the catalytic reaction rate. In the ECO_2RR system, TOFs effectively indicate the catalytic activity near the electrode surface within the reaction-diffusion layer, which is closely related to ESCA (Jiang et al., 2018; Zheng et al., 2019). The electrochemical double-layer capacitance, a basic index for ESCA, was determined to be 8.49 and 7.51 mF/cm^2 for SP_{GDE} and NP_{GDE} respectively, (Fig. S17). These values were consistent with many reported studies and even comparable to some graphite-based matrices (2.56–8.20 mF/cm^2). In electrochemical reactions, a larger ESCA indicated a greater effective area on the electrode for reactions to occur, leading to higher reaction rates and current densities (Jiang et al., 2018; Zheng et al., 2019). In the overall two-electron ECO_2RR process, the rate-determining step at low overpotentials was the electron–proton transfer from the adsorbed CO_2 ($*CO_2^{\cdot-}$) to the *COOH intermediate. The Tafel slope for CO_2 to CO conversion catalyzed by SP_{GDE} was 171 mV/dec, suggesting that single electron transfer is the rate-limiting step, which may involve the generation of $*CO_2^{\cdot-}$, *COOH, or both (Fig. 5(b)). This indicates that CO_2 adsorption and activation on the SP_{GDE} surface occur relatively rapidly (Jiang et al., 2018; Zheng et al., 2019; Liu et al., 2021).

At high current densities, SP_{GDE} exhibited excellent performance in MEA (Fig. S18). Particularly, the CO_2 to CO conversion rate rapidly increased above a 2.0-V cell voltage and maintained a high FE_{CO} (> 90%) across a wide range of current densities between 10 and 50 mA/cm^2 (Fig. 5(c)). These values correspond to an energy efficiency of > 50% (Fig. 5(d)). As the current further increased to 70 mA/cm^2, CO selectivity remained stable at 77%. The relatively stable CO selectivity after 8 h of high current operation coupled with nearly unchanged chemical properties of SP_{GDE} indicated the stability of SP_{GDE} (Figs. 5(e) and S19). Despite some changes in FTIR and XRD spectra (Fig. S19) owing to the unwashed $KHCO_3$, most chemical bonds exhibit minimal changes after electrolysis, confirming the effective protection of Ni SACs in SP_{GDE}.

4 Conclusions

A Ni SACs-laden GDE is fabricated using waste SP protein and Ni from wastewater through electrospinning. The resulting material exhibits excellent activity for CO_2 to CO electro-conversion. The SP protein in wastewater effectively pre-anchors

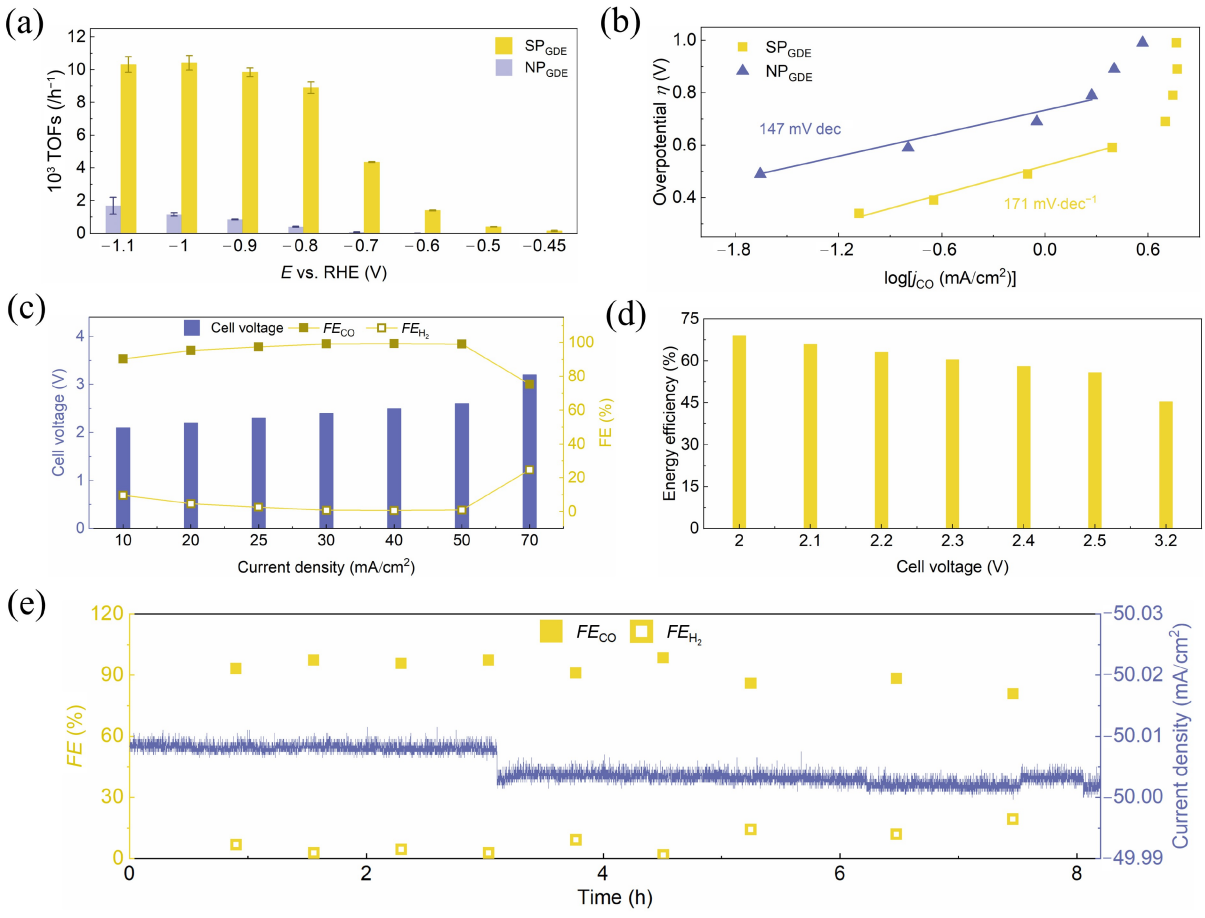

Fig. 5 ECO_2RR performance of SP_{GDE} in a MEA. (a) TOFs and (b) Tafel plots analysis for CO production by SP_{GDE} and NP_{GDE} catalyzing, (c) and (d) The CO selectivity, cell voltage and energy input in MEA, (e) The long-term stability at 50 mA/cm^2.

Ni ions and enriches nitrogen elements, thereby promoting the formation of N_x–Ni active sites. These sites significantly enhance ECO_2RR performance, achieving a maximum FE_{CO} of 96%. The electrospinning technique is suitable for producing GDE in large quantities, ensuring uniform and controlled exposure of N_x–Ni sites along the GDE nanofibers. This unique architecture and the complex liquid/gas/solid interface formed on the GDE surface enable high current operation (90% FE_{CO} at 50 mA/cm^2). In addition to facilitating organic waste disposal, the use of GDE-based CO_2 reduction provides additional environmental benefits, such as carbon capture/fixation (478 million tons annually) and HMs recovery (5 million tons annually). This study presents a strategy to address climate change challenges and promote sustainable waste management practices.

Conflict of Interests Lu Lu is a youth editorial board member of *Frontiers of Environmental Science & Engineering*. The authors declare that the research was conducted in the absence of any commercial or financial relationships that could be construed as a potential conflict of interest.

Acknowledgements This work was financially supported by the National Natural Science Foundation of China (No. 22176046), the Science Fund for Creative Research Groups of the National Natural Science Foundation of China (No. 52321005), the Shenzhen Science and Technology Program (Nos. KQTD20190929172630447, JCYJ20210324124209025, and GXWD20220811173949005), and the Natural Science Foundation of Guangdong Province (No. 2022A1515012016).

Electronic Supplementary Material Supplementary material is available in the online version of this article at https://doi.org/10.1007/s11783-025-1974-y and is accessible for authorized users.

References

Blundell T L, Jenkins J A (1977). The binding of heavy metal to proteins. Chemical Society Reviews, 6(2): 139–171

Fan L, Xia C, Zhu P, Lu Y, Wang H (2020). Electrochemical CO_2

reduction to high-concentration pure formic acid solutions in an all-solid-state reactor. Nature Communications, 11(1): 3633

Ge J, Lei J, Zare R N (2012). Protein-inorganic hybrid nanoflowers. Nature Nanotechnology, 7(7): 428–432

Gu C H, Pan Y, Wei T T, Zhang A Y, Si Y, Liu C, Sun Z H, Chen J J, Yu H Q (2024). Upcycling waste sewage sludge into superior single-atom Fenton-like catalyst for sustainable water purification. Nature Water, 2(7): 649–662

Gustavsson J, Cederberg C, Sonesson U, Otterdijk R, Meybeck A (2011). Global Food Losses and Food Waste-Extent, Causes and Prevention. Rome: Food and Agriculture Organization of the United Nations

Jiang K, Siahrostami S, Zheng T, Hu Y, Hwang S, Stavitski E, Peng Y, Dynes J, Gangisetty M, Su D, et al. (2018). Isolated Ni single atoms in graphene nanosheets for high-performance CO_2 reduction. Energy & Environmental Science, 11(4): 893–903

Jones N (2013). Troubling milestone for CO_2. Nature Geoscience, 6(8): 589

Li T, Lees E W, Goldman M, Salvatore D A, Weekes D M, Berlinguette C P (2019). Electrolytic conversion of bicarbonate into CO in a flow cell. Joule, 3(6): 1487–1497

Li Z, He D, Yan X, Dai S, Younan S, Ke Z, Pan X, Xiao X, Wu H, Gu J (2020). Size-dependent nickel-based electrocatalysts for selective CO_2 reduction. Angewandte Chemie International Edition, 59(42): 18572–18577

Liang S, Jiang Q, Wang Q, Liu Y (2021). Revealing the real role of nickel decorated nitrogen-doped carbon catalysts for electrochemical reduction of CO_2 to CO. Advanced Energy Materials, 11(36): 2101477

Liu C, Wu Y, Sun K, Fang J, Huang A, Pan Y, Cheong W C, Zhuang Z, Zhuang Z, Yuan Q, et al. (2021). Constructing FeN_4/graphitic nitrogen atomic interface for high-efficiency electrochemical CO_2 reduction over a broad potential window. Chem, 7(5): 1297–1307

Liu Y, Li H, Chen S, Zhang L, Li S, Lv H, Gao J, Cui S, Jiang K (2024). Synergetic pathways of water-energy-carbon in ecologically vulnerable regions aiming for carbon neutrality: a case study of Shaanxi, China. Frontiers of Environmental Science & Engineering, 18: 106

Lu L, Guest J S, Peters C A, Zhu X, Rau G H, Ren Z J (2018). Wastewater treatment for carbon capture and utilization. Nature Sustainability, 1(12): 750–758

Mohareb E A, Heller M C, Guthrie P M (2018). Cities' role in mitigating united states food system greenhouse gas emissions. Environmental Science & Technology, 52(10): 5545–5554

Nguyen T N, Dinh C T (2020). Gas diffusion electrode design for electrochemical carbon dioxide reduction. Chemical Society Reviews, 49(21): 7488–7504

Peng C, Luo G, Zhang J, Chen M, Wang Z, Sham T K, Zhang L, Li Y, Zheng G (2021). Double sulfur vacancies by lithium tuning enhance CO_2 electroreduction to n-propanol. Nature Communications, 12(1): 1580

Qin J, Wang Q, Han B, Jin C, Luo C, Sun Y, Dai Z, Wang S, Liu H, Zheng X, et al. (2025). Heterogeneous Fe–Ni dual-atom catalysts coupled N-vacancy engineering for enhanced activation of peroxymonosulfate. Applied Catalysis B: Environment and Energy, 360: 124538

Reichstein M, Riede F, Frank D (2021). More floods, fires and cyclones-plan for domino effects on sustainability goals. Nature, 592(7854): 347–349

Sharifian R, Wagterveld R M, Digdaya I A, Xiang C, Vermaas D A (2021). Electrochemical carbon dioxide capture to close the carbon cycle. Energy & Environmental Science, 14(2): 781–814

Sun J, Tu R, Xu Y, Yang H, Yu T, Zhai D, Ci X, Deng W (2024). Machine learning aided design of single-atom alloy catalysts for methane cracking. Nature Communications, 15(1): 6036

Sun M, Guan W, Chen C, Wu C, Liu X, Meng B, Chen T, Han Y, Wang J, Xi S, et al. (2025). Mechanistic insight into the synergy between nickel single atoms and nanoparticles on N-doped carbon for electroreduction of CO_2. Journal of Energy Chemistry, 100: 327–336

Tan A, Zhao F, Zhang Y, Li G, Wu C, Liu Z, Li J, Liu J (2025). Innovative application of transfer learning on small-scale datasets: analysis and optimization of catalyst ink for the low-iridium membrane electrode assemblies of proton exchange membrane water electrolysis. Chemical Engineering Science, 302: 120814

Verma S, Kim B, Jhong H R M, Ma S, Kenis P J A (2016). A gross-margin model for defining technoeconomic benchmarks in the electroreduction of CO_2. ChemSusChem, 9(15): 1972–1979

Voosen P (2020). The hunger forecast. Science, 368: 226–229

Wang W, Shao C, Feng Y, Cheng Y (2024). Effect of single atom loading on the CO_2 reduction activity of pure and defective W_2CO_2 MXene. Molecular Catalysis, 569: 114550

Weekes D M, Salvatore D A, Reyes A, Huang A, Berlinguette C P (2018). Electrolytic CO_2 Reduction in a flow cell. Accounts of Chemical Research, 51(4): 910–918

Weng S, Xu Y (2016). Analysis of Fourier Transform Infrared Spectroscopy (3rd edition). Beijing: Chemical Industry Press (in Chinese)

Xia C, Zhu P, Jiang Q, Pan Y, Liang W, Stavitski E, Alshareef H N, Wang H (2019). Continuous production of pure liquid fuel solutions via electrocatalytic CO_2 reduction using solid-electrolyte devices. Nature Energy, 4(9): 776–785

Xu X, Sharma P, Shu S, Lin T S, Ciais P, Tubiello F N, Smith P, Campbell N, Jain A K (2021). Global greenhouse gas emissions from animal-based foods are twice those of plant-based foods. Nature Food, 2(9): 724–732

Yang H, Lin Q, Zhang C, Yu X, Cheng Z, Li G, Hu Q, Ren X, Zhang Q, Liu J, et al. (2020). Carbon dioxide electroreduction on single-atom nickel decorated carbon membranes with industry compatible current densities. Nature Communications, 11(1): 593

Yang H, Wu Y, Li G, Lin Q, Hu Q, Zhang Q, Liu J, He C (2019). Scalable production of efficient single-atom copper decorated carbon membranes for CO_2 electroreduction to methanol. Journal of the American Chemical Society, 141(32): 12717–12723

Yang M, Li X, Chao W, Gao X, Wang H, Lu L (2024). Renewable biosynthesis of isoprene from wastewater through a synthetic biology approach: the role of individual organic compounds. Frontiers of Environmental Science & Engineering, 18: 28

Yao R, Sun K, Zhang K, Wu Y, Du Y, Zhao Q, Liu G, Chen C, Sun Y, Li J (2024). Stable hydrogen evolution reaction at high current densities via designing the Ni single atoms and Ru nanoparticles linked by carbon bridges. Nature Communications, 15(1): 2218

Ye C, Guo Z, Zhou Y, Shen Y (2025). Nickel-based dual single atom electrocatalysts for the nitrate reduction reaction. Journal of Colloid and Interface Science, 677: 933–941

Yuan X, Zhang X, Yang Y, Li X, Xing X, Zuo J (2024). Emission of greenhouse gases from sewer networks: field assessment and isotopic characterization. Frontiers of Environmental Science & Engineering, 18: 119

Zheng T, Jiang K, Ta N, Hu Y, Zeng J, Liu J, Wang H (2019). Large-scale and highly selective CO_2 electrocatalytic reduction on nickel single-atom catalyst. Joule, 3(1): 265–278